https://doi.org/10.5194/egusphere-2026-3464
Preprint. Discussion started: 17 August 2026

Firn Rheology Revealed by Contrasting Shear Regimes

Aslak Grinsted[1], Nicholas Mossor Rathmann[1], Johannes Freitag[2], Josephine Lindsey-Clark[1], Sune Olander Rasmussen[1], Niels Fabrin Nymand[1], and Christine Schøtt Hvidberg[1]

[1]Physics of Ice, Climate, and Earth, Niels Bohr Institute. University of Copenhagen, Jagtvej 128, DK-2200 Copenhagen N, Denmark

[2]Alfred Wegener Institute, Helmholtz Centre for Polar and Marine Research, Bremerhaven, Germany

Correspondence: Aslak Grinsted (aslak@nbi.ku.dk)

Abstract. Firn densification is commonly modelled using 1D column approaches that neglect the deformation history associated with ice flow. Here, we present a flowline firn model that explicitly accounts for the accumulation and horizontal strain experienced by firn along its trajectory and use it to infer density-dependent rheology directly from observations.

Applying the method to two ice-core sites in northeast Greenland with contrasting strain regimes, we constrain both the total densification response and its partitioning into shear and volumetric components. While steady-state and flowline inversions agree at large scales, the combined function governing vertical strain is tightly constrained, whereas individual rheological parameters remain poorly identifiable.

The inferred rheology departs markedly from standard formulations, with enhanced near-surface densification, reduced viscous Poisson ratios, and pronounced non-monotonic structure. These behaviours are incompatible with a single power-law rheology and instead require the combined action of multiple deformation mechanisms, including grain-size-dependent creep and evolving anisotropy. The resulting parameters should therefore be interpreted as effective representations of these processes.

These results further imply that firn-derived gas proxies such as Δage and δ^{15}N may contain a dynamical component linked to horizontal strain, with potential implications for the interpretation of ice-core chronologies.

1 Introduction

Firn densification governs the transformation of snow into solid ice in the upper layers of glaciers and ice sheets. As snow accumulates, increasing overburden stress drives progressive compaction until the density approaches that of incompressible glacier ice. This process exerts a primary control on surface elevation change and on the trapping of atmospheric gases, including the close-off depth and the gas–ice age difference (Δage), and thereby strongly influences the interpretation of ice-core records. It also affects additional archive processes such as isotopic diffusion in the firn column and the thinning and preservation of annual layers (Arthern and Wingham, 1998; Schwander and Stauffer, 1984; Buizert et al., 2015; Stevens et al., 2020).

The mechanical response of firn has long been recognized to depend on the full stress state. Early laboratory and theoretical studies demonstrated that deformation reflects a combination of volumetric compression and shear, and introduced concepts

https://doi.org/10.5194/egusphere-2026-3464
Preprint. Discussion started: 17 August 2026

such as compressibility, shear viscosity, and viscous Poisson ratio to describe snow as a porous compressible material (Bader, 1962; Mellor and Smith, 1966; Salm, 1967; Mellor, 1974). These formulations emphasize that deformation depends on the stress invariants rather than on overburden pressure alone, providing a natural framework for separating volumetric and deviatoric contributions to densification.

Despite this early understanding, most firn densification models remain effectively one-dimensional. Classical formulations, such as the empirical model of Herron and Langway Jr (1980), relate densification primarily to temperature and accumulation rate, implicitly assuming that vertical compression under overburden stress dominates the process. More physically based models incorporate mechanisms such as grain-boundary sliding, sintering, and power-law creep (Arthern et al., 2010; Goujon et al., 2003; Barnola et al., 1991), alongside detailed snowpack formulations that resolve near-surface processes and grain-scale physics (Bartelt and Lehning, 2002; Vionnet et al., 2012). Earlier work emphasized specific mechanisms such as grain-boundary sliding (Alley, 1987) and multi-stage physical models (Arnaud et al., 2000). However, these approaches typically retain a one-dimensional formulation and therefore do not account for the evolving stress state associated with ice flow. Intercomparisons reveal substantial spread in modeled densification rates under identical forcing, highlighting persistent uncertainties in model formulation (Lundin et al., 2017). Continuum formulations that explicitly couple deviatoric and volumetric stresses have been developed for firn rheology (Gagliardini and Meyssonnier, 1997), but are not widely used in this context.

Observations from dynamically active regions challenge this simplified picture (Vallelonga et al., 2014; Riverman et al., 2019). In regions of strong horizontal velocity gradients, such as ice-stream shear margins, shear deformation can enhance grain rearrangement and creep, leading to accelerated densification that cannot be explained by vertical loading alone. Modeling studies suggest that horizontal strain rates contribute through mechanisms such as strain softening and enhanced creep deformation (Oraschewski and Grinsted, 2022; Arrizabalaga-Iriarte et al., 2025). At the same time, microstructure-based models indicate that firn densification cannot be captured by a single rheological law, but instead reflects the combined action of multiple deformation mechanisms (e.g. Arnaud et al., 2000; Salamatin et al., 2009).

Constraining firn rheology from observations is challenging because a single site provides limited information on deformation mechanisms. Density profiles from low-strain sites primarily constrain the vertically integrated response to overburden stress, leaving the partitioning between volumetric and shear deformation poorly resolved. The EastGRIP region of the Northeast Greenland Ice Stream provides a natural experiment to overcome this limitation: sites within the ice stream and its adjacent shear margins experience similar climatic forcing but contrasting strain regimes. This configuration allows shear and thermodynamic effects to be disentangled, providing complementary constraints on the rheology.

This apparent disconnect between the classical understanding of firn as a stress-dependent, compressible material and its predominantly one-dimensional, vertically resolved representation in large-scale models motivates the development of frameworks that explicitly incorporate the full stress state and constrain rheology directly from observations.

Here, we present a flowline firn model based on Gagliardini and Meyssonnier (1997) that accounts for both accumulation and horizontal strain along ice column trajectories, and use it to infer density-dependent rheology directly from density profiles. Using observations from two cores in northeast Greenland with contrasting strain regimes but similar climatic forcing, we separate volumetric and shear contributions to densification. We show that overburden stress alone cannot reproduce the observed

https://doi.org/10.5194/egusphere-2026-3464
Preprint. Discussion started: 17 August 2026

density profiles and that shear exerts a first-order control on the depth–density relationship. These results demonstrate that accounting for the full stress state is essential for modeling firn structure and interpreting density observations in dynamically evolving settings.

2 Data

We use density measurements from two firn cores in the EastGRIP region: one located within the North East Greenland Ice Stream (NEGIS) at the EastGRIP site, and one located in the adjacent shear margin (Fig. 1). The EastGRIP density measurements were obtained through detailed logging of core dimensions and weight under carefully controlled conditions in a snow cave, supplemented by pit measurements (Rasmussen et al., 2023). The S5-1 density profile was derived from X-ray computed tomography (HXCT), as described by Bagherzadeh et al. (2024). To this end, 1-meter-long ice core segments were scanned using the AWI-iceCT in helical flyby mode at a resolution of 120 μm. The segmentations of the three-dimensional firn reconstructions were adjusted to match the measured weights; this enables precise density estimates that are independent of core quality and applicable even to low-porosity ice.

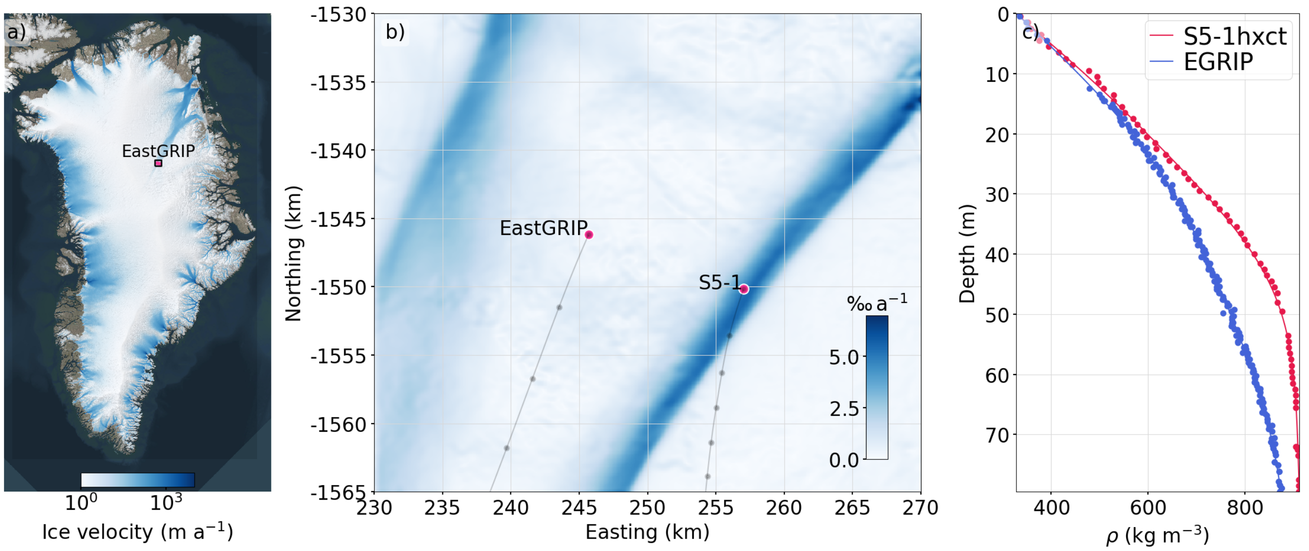

Figure 1. a) Ice-flow velocities (Joughin et al., 2018) of the Greenland ice sheet showing the location of the EastGRIP ice-core camp within the Northeast Greenland Ice Stream. b) Effective strain rates calculated from Sentinel-1 InSAR velocities (Andersen et al., 2020) in the neighborhood of the EastGRIP camp and location of the two ice-core locations. Back-trajectories calculated from the present-day flow field are shown with a dot per century. c) The density measurements and smoothed profiles at the two sites used in this study.

We estimate the measurement uncertainty and how it varies with depth from the scatter around a smoothed version of the observed density profiles (Fig. 1c). The smoothed profiles are obtained by fitting a generalized additive model using pyGAM

https://doi.org/10.5194/egusphere-2026-3464
Preprint. Discussion started: 17 August 2026

with monotonically increasing concave constraints (Servén et al., 2025). The intuition behind the concave constraint is that the densification rate slows down as the firn becomes more dense.

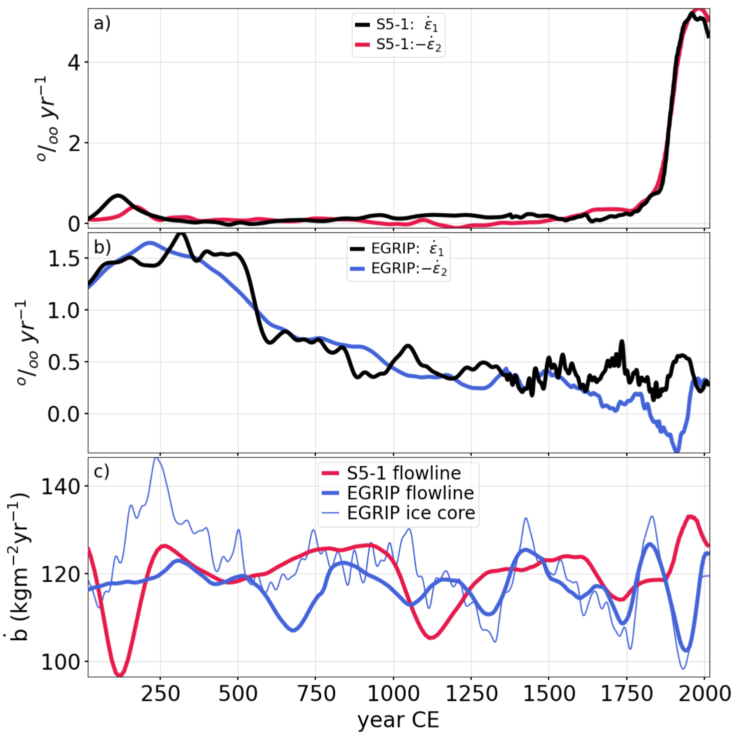

Figure 2. Principal strain rates $\dot{\epsilon}_1$, $\dot{\epsilon}_2$ (a,b) and accumulation rates $\dot{b}$ (c) extracted along the back-trajectories for the EastGRIP and S5-1 sites. The value of $-\dot{\epsilon}_2$ is plotted to facilitate direct comparison with $\dot{\epsilon}_1$ and to clearly distinguish flow divergence. Present-day radar+DEM based regional accumulation rates (thick lines) are compared to those inferred from the EastGRIP icecore timescale (thin blue) (see appendix A). The ice-core accumulation rate has been smoothed with a 10-year gaussian filter.

Horizontal strain rates (Fig. 2) and particle back-trajectories (Fig. 1) are derived from AWI TerraSAR-X velocity fields (Hvidberg et al., 2020), supplemented upstream by DTU Sentinel-1 interferometric velocities (Hvidberg et al., 2020; Andersen et al., 2020). Back-trajectories are shown over a 2000-year period; however, firn at 100 m depth at EastGRIP was deposited approximately 700 years ago (Sinnl et al., 2022), such that only the more recent portion is relevant for the present analysis. Prior to strain-rate calculation, the TerraSAR-X and Sentinel-1 velocity fields are smoothed using Gaussian filters with characteristic length scales of 250 m and 500 m, respectively. These values are guided by previous validation of the velocity products (Hvidberg et al., 2020), which showed that modest smoothing is required to suppress noise, particularly for lower-resolution datasets. Because strain-rate estimates involve spatial derivatives and are therefore more sensitive to noise than velocities, slightly more conservative smoothing is applied here. The chosen values represent a compromise between noise reduction and spatial resolution, and the results are not sensitive to reasonable variations in the smoothing length scale. The high spatial

https://doi.org/10.5194/egusphere-2026-3464
Preprint. Discussion started: 17 August 2026

resolution of these interferometric products makes them well suited for resolving strain-rate gradients across the shear margin. The accumulation history along each back-trajectory is obtained by interpolating positions into the spatial accumulation field described in appendix A.

The two sites are located within 15 km of each other and are therefore subject to very similar meteorological conditions. We consequently assume a constant accumulation rate at both sites in the steady-state modelling below, based on the millennial-average accumulation rate derived from the EastGRIP ice core (Appendix A). Temperature profiles have been measured with high precision at both sites and exhibit very similar vertical structure. Over the common depth interval of 15–95 m, mean temperatures are $-31.1\,^{\circ}\mathrm{C}$ near EastGRIP (measured $\sim$2 km from the drilling site) and $-30.9\,^{\circ}\mathrm{C}$ at S5-1, corresponding to a difference of less than $0.3\,^{\circ}\mathrm{C}$. Given this small offset, a constant temperature of $-31\,^{\circ}\mathrm{C}$ is adopted as a representative value for both sites. The seasonal amplitude of surface temperature is estimated to be 32 K from a sinusoidal fit to PROMICE observations at EastGRIP (Fausto et al., 2021; How et al., 2022).

3 Model

3.1 Rheology

We build on the Gagliardini and Meyssonnier (1997) model (GM97), a continuum formulation for porous ice that applies power-law creep to compressible firn. This describes firn rheology that seamlessly conforms to an incompressible solid-ice power-law rheology in the limit where the density (ρ) approaches that of solid ice ($\rho_{\mathrm{ice}} = 921\,\mathrm{kg\,m^{-3}}$). A starting point for the model is therefore a reference solid-ice rheology, or flow law, relating the strain-rate $\dot{\boldsymbol{\epsilon}}$ to the deviatoric stress $\boldsymbol{\tau} = \boldsymbol{\sigma} + \boldsymbol{I}p$, where $p = -\mathrm{tr}(\boldsymbol{\sigma})/3$. Here, we use the canonical Glen rheology for ice (Glen, 1955)

$$\dot{\boldsymbol{\epsilon}}_{\mathrm{ice}} = A\tau_e^{n-1}\boldsymbol{\tau}\ , \tag{1}$$

where the fluidity is governed by the effective deviatoric stress ($\tau_e^2 = \frac{1}{2}\boldsymbol{\tau} : \boldsymbol{\tau}$) with a flow law exponent n, and a temperature-dependent rate factor A. We assume a conventional Arrhenius-style rate factor of the form $A(T) = A_0 e^{-Q/RT}$ where T is temperature, R is the universal gas constant, Q is an activation energy.

Solid ice is incompressible and therefore responds only to deviatoric stresses. In contrast, porous firn can be compressed under pressure, and this compressive deformation must also affect the fluidity, as recognized in early continuum descriptions of firn as a compressible viscous material (Bader, 1962; Mellor and Smith, 1966). The GM97 model accounts for this by taking the effective stress σ_E to depend on both the deviatoric stress and pressure, consistent with plastic potential theory:

$$\sigma_E^2 = a\tau_e^2 + \frac{1}{3}bp^2\ , \tag{2}$$

where a is the firn shear enhancement factor, and b is the compressibility[1], both of which we assume depends only on ρ. In the limit of solid ice we would expect $a \to 1$ and $b \to 0$. Assuming a power-law relationship between the effective strain rate and

[1]Note that our definition of b follows Arrizabalaga-Iriarte et al. (2025) which deviates from the convention used in Gagliardini and Meyssonnier (1997) by a factor 3

https://doi.org/10.5194/egusphere-2026-3464
Preprint. Discussion started: 17 August 2026

effective stress, the porous rheology can be derived to be (Duva and Crow, 1994; Arrizabalaga-Iriarte et al., 2025)

$$\dot{\boldsymbol{\epsilon}} = A\sigma_E^{n-1}\left(a\boldsymbol{\tau} - \frac{2}{9}bp\boldsymbol{I}\right) . \tag{3}$$

This rheology ensures that deviatoric stresses produce deviatoric strain rates, while pressure produces compression, and either influence the fluidity.

Arrizabalaga-Iriarte et al. (2025) derived the corresponding inverse rheology, expressing stress in terms of strain rate:

$$\boldsymbol{\sigma} = A^{-1/n}\dot{\epsilon}_e^{(1-n)/n}\left[\frac{1}{a}\left(\dot{\boldsymbol{\epsilon}} - \frac{\mathrm{tr}(\dot{\boldsymbol{\epsilon}})}{3}\boldsymbol{I}\right) + \frac{3}{2b}\mathrm{tr}(\dot{\boldsymbol{\epsilon}})\,\boldsymbol{I}\right] , \tag{4}$$

where the effective strain rate depends on the first and second invariants of the strain-rate tensor, $\mathrm{tr}(\dot{\boldsymbol{\epsilon}})$ and $\dot{\boldsymbol{\epsilon}} : \dot{\boldsymbol{\epsilon}}$, and is

$$\dot{\epsilon}_e^2 = \frac{1}{2a}\left(\dot{\boldsymbol{\epsilon}} : \dot{\boldsymbol{\epsilon}} - \frac{1}{3}\mathrm{tr}(\dot{\boldsymbol{\epsilon}})^2\right) + \frac{3}{4b}\mathrm{tr}(\dot{\boldsymbol{\epsilon}})^2 . \tag{5}$$

The coefficient functions $a(\rho)$ and $b(\rho)$ can be estimated directly from deformation tests on firn subject to simple shear (constraining a) and bulk compression (constraining b). However, a more convenient way is to consider an unconfined compression test where only σ_{zz} is non-zero. In this case, it is useful to express the problem in terms of the apparent viscous Poisson ratio and compressive viscosity (see also Mellor and Smith, 1966; Mellor, 1974; Shinojima, 1967)

$$\nu_v \equiv -\frac{\dot{\epsilon}_{xx}}{\dot{\epsilon}_{zz}} = \frac{9a-2b}{18a+2b} , \tag{6}$$

$$\eta_E \equiv \frac{\sigma_{zz}}{\dot{\epsilon}_{zz}} = A^{-1}\left(\frac{a\,\sigma_{zz}^2}{3} + \frac{b\,\sigma_{zz}^2}{27}\right)^{\frac{1-n}{2}} \frac{27}{18a+2b} . \tag{7}$$

Thus, an unconfined compression experiment yielding $\dot{\epsilon}_{xx}$ and $\dot{\epsilon}_{zz}$ for a given σ_{zz} and ρ provides exactly the information needed to determine both $a(\rho)$ and $b(\rho)$.

3.2 1D Formulation

We seek to build a Lagrangian column model of firn, based on the GM97 rheology, that can readily be integrated into existing 1D densification modelling frameworks which rely on mass conservation for time evolution (e.g. Stevens et al., 2020)

$$\frac{D\rho}{Dt} + \rho\,\mathrm{tr}(\dot{\boldsymbol{\epsilon}}) = 0 . \tag{8}$$

Horizontal strain and vertical shear strain are typically disregarded in existing 1D models. Here, we relax this constraint by neglecting only vertical shear, allowing the strain-rate tensor to be written in terms of its horizontal principal strain rates $\dot{\epsilon}_1$ and $\dot{\epsilon}_2$:

$$\dot{\boldsymbol{\epsilon}} = \begin{pmatrix} \dot{\epsilon}_1 & 0 & 0 \\ 0 & \dot{\epsilon}_2 & 0 \\ 0 & 0 & \dot{\epsilon}_{zz} \end{pmatrix} . \tag{9}$$

We assume that $\dot{\epsilon}_1$ and $\dot{\epsilon}_2$ are approximately depth-independent and equal to values derived from remote sensing (satellite-derived surface velocities). Our objective is therefore to determine the vertical strain rate, $\dot{\epsilon}_{zz}$, subject to the assumption that

https://doi.org/10.5194/egusphere-2026-3464
Preprint. Discussion started: 17 August 2026

the vertical stress σ_{zz} is given directly by the overburden load. The problem is therefore partially constrained: we know the horizontal strain-rate components and the vertical stress, but neither the vertical strain rate nor the horizontal stresses.

The problem can be closed using the inverse rheology (Eq. 4) to calculate $\dot{\epsilon}_{zz}$ from σ_{zz}, given the strain-rate tensor in Eq. 9 and setting $n = 3$ (canonical flow exponent). Rearranging the resulting expression, it can be shown that $\dot{\epsilon}_{zz}$ is a solution to the cubic equation

$$k_3\dot{\epsilon}_{zz}^3 + k_2\dot{\epsilon}_{zz}^2 + k_1\dot{\epsilon}_{zz} + k_0 = 0 \,, \tag{10}$$

with coefficients

$$k_3 = -r^3 \tag{11}$$

$$k_2 = \tfrac{1}{2}A\sigma_{zz}^3 r + 3qr^2 \tag{12}$$

$$k_1 = -A\sigma_{zz}^3 q - 3q^2 r \tag{13}$$

$$k_0 = A\sigma_{zz}^3\left[\frac{\dot{\epsilon}_1^2 + \dot{\epsilon}_2^2 - \dot{\epsilon}_1\dot{\epsilon}_2}{3a} + \frac{3(\dot{\epsilon}_1 + \dot{\epsilon}_2)^2}{4b}\right] + q^3 \,, \tag{14}$$

where $r \equiv \frac{2}{3a} + \frac{3}{2b}$ and $q \equiv (\dot{\epsilon}_1 + \dot{\epsilon}_2)\left(\frac{1}{3a} - \frac{3}{2b}\right)$ are convenient shorthands. The vertical strain rate, $\dot{\epsilon}_{zz}$, is obtained as the real root of Eq. 10, which can be found analytically using Cardano's method. The parameter r combines the effects of shear and compressibility and is expected to be more directly constrained by observations than a and b individually. In the special case of vanishing horizontal strain, $\dot{\epsilon}_1 = \dot{\epsilon}_2 = 0$, Eq. 10 reduces to the simple expression

$$\dot{\epsilon}_{zz}\big|_{\dot{\epsilon}_1=\dot{\epsilon}_2=0} = \frac{A\sigma_{zz}^3}{2r^2} \,. \tag{15}$$

3.3 Parameter choices

The coefficient functions $a(\rho)$ and $b(\rho)$ represent relative strain-rate enhancements in firn compared to the reference solid-ice rheology (Glen's law with $n = 3$, Eq. 1). The temperature dependency is asserted to be entirely contained within $A(T)$, modelled using the conventional solid-ice, two-step Arrhenius rate factor

$$A(T) = \max\left(A_\text{cold}\, e^{-Q_\text{cold}/RT},\, A_\text{warm}\, e^{-Q_\text{warm}/RT}\right) \,, \tag{16}$$

with a transition between the cold and warm regimes occurring at approximately $T \approx 263\,\mathrm{K}$. Here, R is the universal gas constant, $Q_\text{cold} = 60$ kJ mol^{-1} and $Q_\text{warm} = 139$ kJ mol^{-1} are two activation energies, and $A_\text{cold} = 3.985 \times 10^{-13}$ s^{-1} Pa^{-3} and $A_\text{warm} = 1.916 \times 10^3$ s^{-1} Pa^{-3} are pre-factors taken from Greve and Blatter (2009). We consider this a local approximation to a more physically complete solid-ice rheology (Fan et al., 2025; Goldsby and Kohlstedt, 2001). The enhancements a and b provide flexibility to partially compensate for biases in the reference ice rheology.

Unconfined laboratory experiments on snow/firn shows that the flow exponent deviates strongly for axial stresses below ~ 25 kPa (Mellor and Smith, 1966). This suggests that the GM97 model with a fixed exponent of $n = 3$ might struggle to capture the physics in the top 5 m of the firn column. Indeed, models designed to capture near-surface processes commonly use

https://doi.org/10.5194/egusphere-2026-3464
Preprint. Discussion started: 17 August 2026

a flow exponent of $n = 1$ (Bartelt and Lehning, 2002; Vionnet et al., 2012). Interestingly, this is similar to the flow exponents found for grain-size-sensitive creep in solid ice (Goldsby, 2006; Fan et al., 2025), but we note that the grain-size exponents used in firn models are incompatible with the exponents found for solid ice.

Several studies have calibrated the coefficients $a(\rho)$ and $b(\rho)$ to density profiles from different sites, but have reported inconsistent estimates (Gagliardini and Meyssonnier, 1997; Zwinger et al., 2007; Arrizabalaga-Iriarte et al., 2025). This inconsistency arises because determining both parameters from estimates of $\dot{\epsilon}_{zz}$ at a single site is ill-posed (see Eq. 10), motivating the need for incorporating additional physically informed constraints on a and b.

In the solid-ice limit $\rho \to \rho_{\text{ice}}$, the firn should behave as an incompressible material with a viscous Poisson ratio of $\nu_v = 1/2$. Conversely, in the low-density regime ($\rho \to 0$), firn should compress without horizontal expansion so that $\nu_v \simeq 0$. Laboratory experiments on unconfined compression indicate that ν_v is close to zero for $\rho < 300\ \mathrm{kg\,m^{-3}}$ (Shinojima, 1967). These constraints suggest that $\nu_v(\rho)$ increases monotonically with density. Classical interpretations, such as Mellor (1974), argue for a sigmoidal-like transition between these limits as $\rho \to \rho_{\text{ice}}$. Rather than prescribing a specific functional form, our approach is instead to allow the underlying rheological parameters $a(\rho)$ and $b(\rho)$ to vary freely, from which $\nu_v(\rho)$ emerges implicitly.

3.4 Steady-state

In steady state, the mass fluxes into and out of the firn column must balance. The mass flux through the surface is the accumulation rate $\dot{b}$, and the column loses mass through its sides under divergent flow. The flux through the bottom immediately follows from closing the balance, giving

$$w(z) = \frac{\dot{b} - M(z)\,(\dot{\epsilon}_{xx} + \dot{\epsilon}_{yy})}{\rho(z)}\,, \tag{17}$$

where the overburden load per area at depth z of a firn column is

$$M(z) = \int_0^z \rho(z)\,dz\,. \tag{18}$$

The steady vertical density gradient $\partial\rho/\partial z$ then follows from the *local* mass-conservation equation

$$w\frac{\partial \rho}{\partial z} + \rho(\dot{\epsilon}_{xx} + \dot{\epsilon}_{yy} + \dot{\epsilon}_{zz}) = 0\,, \tag{19}$$

combined with the expressions for w and $\dot{\epsilon}_{zz}$.

We compute the steady density profile by numerically integrating $\partial\rho/\partial z$ from the surface down to depth. In doing so, seasonal temperature variability is incorporated through its influence on the densification rate via $A(T)$, following the approach described in Appendix B. The full numerical procedure used to obtain the steady-state profile is outlined in Appendix C.

4 Methods

Our aim is to invert the two firn-density profiles for $a(\rho)$ and $b(\rho)$. We do that using two separate approaches. In the first approach, we consider the special case of steady forcing, where every firn parcel has experienced constant horizontal strain

https://doi.org/10.5194/egusphere-2026-3464
Preprint. Discussion started: 17 August 2026

rates throughout its entire history since deposition. In the second approach, a flowline model is built where every parcel is tracked since deposition and subject to time-dependent horizontal strain rates, calculated along present-day back-trajectories.

4.1 Steady approach

We determine the coefficient functions $a(\rho)$ and $b(\rho)$ without running the model for the full profile, deriving them instead directly from the gradient of the smoothed density observations. For each site, we identify the depth z corresponding to a given ρ, integrate the density profile to obtain $M(z)$ and thus $\sigma_{zz}(z)$, and estimate the local density gradient $\partial\rho/\partial z|_{z(\rho)}$. Combined with site specific conditions $\dot{b}$, $\dot{\epsilon}_1$, $\dot{\epsilon}_2$, and the depth-average temperature T_m, equations 17 and 19 yield $w(z)$ and $\dot{\epsilon}_{zz}$ at both sites. We then determine a and b by minimizing the least-squares misfit between the model (Eq. 10) and the two observational estimates of $\dot{\epsilon}_{zz}$, subject to the constraint that $\nu_v \in [0, \frac{1}{2}]$. In this approach, we do not account for temperature variability but simply assume a constant rate factor, $A(T_m)$.

We compute the local density gradient $\partial\rho/\partial z$ directly from the smoothed density profiles shown in Fig. 1. Because the inversion relies only on this local gradient and the overburden stress (obtained by integrating the observed density profile), both $a(\rho)$ and $b(\rho)$ can be constrained independently at each density. In particular, the inferred values at a given ρ do not depend on the model fit at other depths.

4.2 Non-steady flowline approach

When applying the model along flowlines, each observed density profile reflects the integrated deformation and deposition history experienced by a firn column. Horizontal strain rates and accumulation histories are prescribed from external datasets, and the inversion solves for rheological parameters that best reproduce the observed profiles under this time-dependent forcing for $\dot{b}$, $\dot{\epsilon}_1$, and $\dot{\epsilon}_2$ (reconstructed by sampling spatial fields along back-trajectories; Fig. 2). Details of the numerical implementation are given in Appendix D.

We model $\log(a(\rho))$ and $\nu_v(\rho)$ as splines with 14 degrees of freedom each, and calculate $b(\rho)$ using Eq. 6. Since this model is very flexible, we regularize the splines to avoid overfitting. Furthermore, because the inversion is weakly constrained at depth and at low densities, we impose regularization that reflects prior physical expectations about firn rheology. Laboratory creep and compression experiments on snow and firn consistently demonstrate that material stiffness and effective viscosity increase monotonically with density. Uniaxial compression tests performed under controlled stress and temperature conditions show a smooth strengthening of snow and firn with increasing density, with no evidence for local softening or inflection behavior (Mellor and Smith, 1966; Mellor, 1974; Chandel et al., 2007). These results are supported by modern microstructure-based simulations, which confirm that firn densification reflects the progressive stiffening of a porous polycrystalline ice matrix (Fourteau et al., 2024). Local concave curvature in inferred $\log(a(\rho))$ would therefore imply unphysical weakening with compaction that is not supported by laboratory observations.

Our imposed regularization term therefore penalizes negative curvature in the spline coefficients describing $\log(a(\rho))$. This regularization acts only where the second-order finite difference is concave, while allowing convex curvature where required by the data. This asymmetric regularization encodes a one-sided physical prior, rather than enforcing smoothness *per se*, and

https://doi.org/10.5194/egusphere-2026-3464
Preprint. Discussion started: 17 August 2026

is less restrictive than standard Tikhonov regularization. The total misfit function, minimized by the inversion procedure, is

$$J(\mathbf{m}) = \sum_{i}^{N} \left(\frac{\rho_i - f_i(\mathbf{m})}{\sigma_i} \right)^2 + \lambda \sum_{j=2}^{M-1} \min(\nabla_j^2 \mathbf{c_a}, 0)^2 , \tag{20}$$

where ρ_i are N density observations with uncertainties σ_i, $f_i(\mathbf{m})$ is the forward flowline model evaluated at the corresponding site and depth, $\mathbf{c_a}$ are the spline coefficients representing $\log(a)$, ∇_j^2 denotes a second-order finite-difference operator acting on adjacent coefficients, and λ is a regularization weight.

By penalizing curvature rather than amplitude, this formulation preserves flexibility in the absolute magnitude of $a(\rho)$ while suppressing non-physical structure that is not consistent with observations. The regularization strength λ is chosen such that the reduced χ^2 of the fit is close to unity, ensuring that the solution explains the observations within their uncertainties without overfitting. We verified that the inferred rheological paramters (a and ν_v) is insensitive to the precise value of λ, indicating that the regularization acts primarily to stabilize the inversion rather than to determine the solution.

Because the forward model employs a simplified, single-mechanism rheology, the inferred coefficient function $a(\rho)$ and $b(\rho)$ should be interpreted as effective quantities that reproduce the observed densification rates within this framework. They do not necessarily correspond to intrinsic material properties, but may instead reflect the combined influence of multiple deformation mechanisms and structural effects not explicitly represented in the model.

4.3 Results

The results of the steady and non-steady (flowline) inversions for $a(\rho)$ and $b(\rho)$ are shown in Fig. 3a. Both models provide an excellent fit to the observed density profiles (Fig. 3d,e). The flowline inversion achieves root-mean-square errors of $5\ \mathrm{kg\,m^{-3}}$ for both cores and yields a combined reduced χ^2 of 1.15.

Figure 3a compares the inferred rheological parameters with the reference formulation of Zwinger et al. (2007, Z07). Both inversion approaches require substantially larger enhancement factors than Z07 at low densities, particularly below approximately $500\ \mathrm{kg\,m^{-3}}$, where both a and b exceed the reference values by more than an order of magnitude. The inferred enhancement factors decrease strongly with increasing density. At high densities, the inferred a values become smaller than unity and substantially lower than the Z07 prediction, while b also remains below the reference formulation. The steady-state and flowline inversions agree closely over most of the density range, although some divergence appears near pore close-off where constraints weaken.

The corresponding values of the combined parameter $r = \frac{2}{3a} + \frac{3}{2b}$ are shown in Fig. 3b. In the limit of no horizontal strain, r controls the vertical densification rate for a given rate factor and overburden stress (Eq. 15), making it the most direct point of comparison with conventional one-dimensional densification models such as Herron–Langway. Despite differences between the individual rheological parameters, the steady-state and flowline inversions yield nearly identical estimates of r. Both inversions produce values close to those implied by the classical Herron–Langway densification model over most of the density range. In contrast, the Z07 formulation predicts considerably larger values of r at intermediate and high densities, implying lower densification rates than required to match the observations.

https://doi.org/10.5194/egusphere-2026-3464
Preprint. Discussion started: 17 August 2026

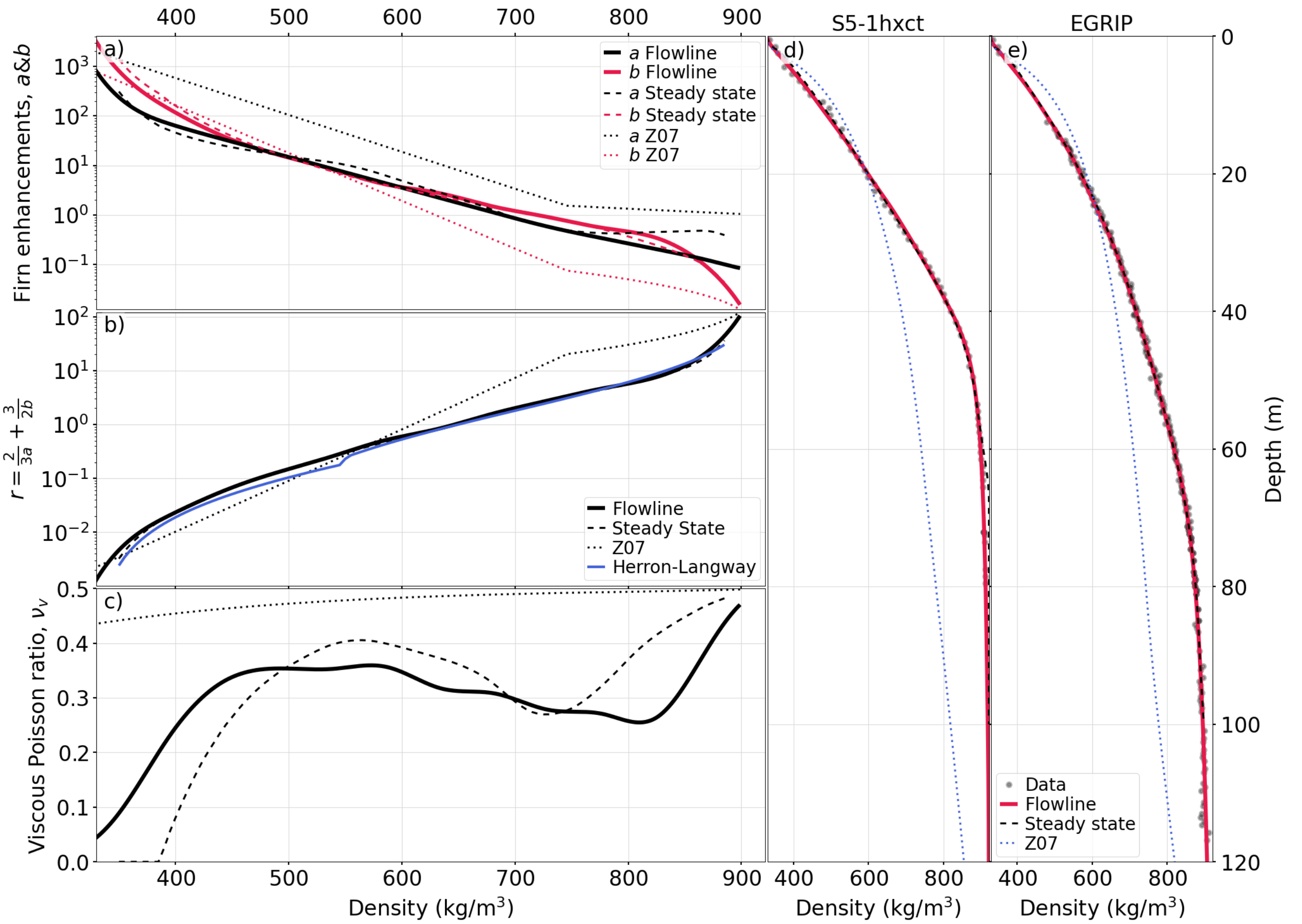

Figure 3. Results of inversion of the firn profiles with the steady-state and flowline models compared to the reference model (Z07; Zwinger et al., 2007). a) shows the shear enhancement $a(\rho)$, and bulk compressibility $b(\rho)$. b) shows the combined parameter r, which controls vertical densification in the no-horizontal-strain limit (Eq. 15). c) shows viscous Poisson ratio $\nu_v(\rho)$. d,e) shows the resulting fit to the observations at the two sites.

The inferred viscous Poisson ratio is shown in Fig. 3c. Both inversions yield values that are systematically lower than those predicted by Z07. The flowline inversion indicates a non-monotonic variation with density, with local maxima near 500–600 $\mathrm{kg\,m^{-3}}$ and reduced values at higher densities before approaching the incompressible limit. The steady-state inversion reproduces the same first-order behaviour but exhibits larger variability at high density.

Figures 3d,e compare the modeled density profiles with observations from the S5-1 and EastGRIP sites. Both inversion approaches reproduce the measured profiles within observational uncertainty over the entire depth range. In contrast, the Z07 parameterization substantially underestimates densification rates, producing density profiles that remain too porous at depth and fail to reproduce the observed approach toward close-off density.

https://doi.org/10.5194/egusphere-2026-3464
Preprint. Discussion started: 17 August 2026

5 Discussion

The steady-state and flowline inversions yield consistent results, pointing to the need for a substantial revision of the reference rheological parameters proposed by (Zwinger et al., 2007, hereafter Z07) in order to reproduce the firn-density profiles near EastGRIP (Fig. 3). By combining data from cores located in two regions with contrasting horizontal strain regimes, the inversion is able to independently constrain both the shear and bulk components of the rheology (i.e., a and b).

In agreement with prior work (Arrizabalaga-Iriarte et al., 2025), we find that a strong enhancement of near-surface compaction is required to match the observed densification rates (see Fig. 3a). In the present formulation, deformation is described using a single power-law rheology with exponent $n = 3$. However, laboratory studies indicate that at low stresses and low densities, firn deformation is more accurately described by a linear, grain-size-dependent viscous mechanism (Mellor and Smith, 1966; Bartelt and Lehning, 2002). This suggests that the total strain rate should be represented as the sum of multiple deformation mechanisms (e.g. Arnaud et al., 2000; Fourteau et al., 2024), with the linear mechanism dominating in the shallow firn (approximately the upper 5 m).

In the absence of such a linear contribution, the model overestimates the effective viscosity in the near surface. The inversion compensates for this structural model deficiency by requiring elevated shear and bulk enhancement factors (a and b). Within the spline-based inversion framework, these parameters are represented as smooth functions of density, allowing the inversion to introduce enhanced rates of deformation at low densities without imposing a specific functional form. The resulting increase in $a(\rho)$ and $b(\rho)$ at low densities should therefore be interpreted, at least in part, as an effective representation of unresolved deformation mechanisms rather than a direct reflection of a single-mechanism rheology.

As the density approaches that of solid ice, we expect the rheology to converge towards that of isotropic polycrystalline ice, with $a \to 1$ and $b \to 0$, consistent with the reference formulation of Zwinger et al. (2007) and the regime in which the analysis of Duva and Crow (1994) applies. However, our inversion yields shear enhancement factors below unity (see Fig. 3a), implying that the inferred firn shear viscosity is higher than that of the reference solid-ice rheology (Eq. 1).

A likely explanation for this discrepancy is that the reference rheology assumes isotropic ice, whereas firn in the shear margin develops a pronounced crystallographic fabric already at depths of $\sim 24\,\mathrm{m}$, as indicated by radar observations showing clear evidence of birefringence loss (Appendix E). This points to the development of a strongly anisotropic fabric with a pronounced horizontal alignment. Such fabrics favor horizontal shear while inhibiting vertical shear and compaction, consistent with the low inferred values of a. This interpretation is consistent with recent microstructure-based studies highlighting the importance of anisotropy and grain-scale processes in firn mechanics (e.g. Fourteau et al., 2024). More generally, this behaviour highlights the limitations of describing high-density firn with an isotropic, single-mechanism rheology, as both anisotropy and evolving pore geometry become increasingly important as pore close-off is approached.

In addition, the inversion becomes increasingly sensitive to data and model uncertainties in this density range. Near pore close-off, small errors in density translate into large changes in inferred rheological parameters due to the rapid variation in bulk compressibility $b(\rho)$. The inferred behaviour at densities above $850\,\mathrm{kg\,m^{-3}}$ should therefore be interpreted with caution, and is best viewed as an effective response within the present model framework rather than a direct estimate of intrinsic ice

https://doi.org/10.5194/egusphere-2026-3464
Preprint. Discussion started: 17 August 2026

rheology. Furthermore, the high-density portion of the profiles corresponds to the deepest and oldest firn, where the assumption of a stationary horizontal flow field (Fig. 1) and a fixed spatial accumulation pattern (Fig. A1) is most likely to break down. However, we note the strong similarity between the accumulation rates inferred from the ice core and those sampled along the flowline back-trajectory of EastGRIP (Fig. 2c). Taken together, this provides strong evidence that the EastGRIP ice-flow velocities and regional accumulation pattern have remained stable over at least the nine centuries.

The viscous Poisson ratio, we determine, is smaller than the Z07 reference rheology across the entire density range (Fig. 3c), and more consistent with expectations expressed in Mellor (1974). However, in contrast to the monotonic behavior suggested in that work, our results indicate a more complex structure.

As shown in Fig. 3c, the viscous Poisson ratio does not increase monotonically with density but instead exhibits pronounced reversals near $\rho \approx 500\ \mathrm{kg\,m^{-3}}$ and $\rho \approx 700\ \mathrm{kg\,m^{-3}}$. We argue that this likely reflects transitions in dominant deformation mechanisms. The first of these occurs close to the canonical transition density of $\rho \approx 550\ \mathrm{kg\,m^{-3}}$ which has previously been identified as a regime shift where the dominant densification mechanisms change from grain rearrangement to deformation of the ice matrix (Herron and Langway Jr, 1980). At higher densities, the additional reversal near $\rho \approx 750\ \mathrm{kg\,m^{-3}}$ is expected as the material must become incompressible ($\nu_v \to 0.5$) as $\rho \to \rho_{\mathrm{ice}}$. The exact shape is influenced by fabric development, evolving pore geometry, and uncertainties in the deepest part of the profiles.

The steady-state and flowline inversions yield qualitatively similar viscous Poisson ratio profiles, although they differ in detail, indicating that $\nu_v(\rho)$ is only weakly constrained by the available data. In contrast, the inferred values of $r(\rho)$ from the two inversions are nearly identical (Fig. 3b). This reflects the central role of r in the vertical strain-rate solution: in the no-horizontal-strain limit it directly controls the relationship between overburden stress and vertical strain rate (Eq. 15), while in the general case it enters the cubic expression for $\dot{\epsilon}_{zz}$ (Eq. 10). Notably, the inferred $r(\rho)$ is also in close agreement with values implied by the classical Herron and Langway Jr (1980) densification model, despite the fundamentally different formulations. This consistency indicates that r captures the effective bulk response of firn densification, while the present framework provides additional insight into its partitioning between shear and volumetric contributions.

This behavior can be understood from the no-horizontal-strain limit of the model (Eq. 15); in regions with negligible horizontal strain, densification and vertical strain depend primarily on r, making it the dominant rheological control on the model response. Consequently, $r(\rho)$ is tightly constrained by the observations, whereas trade-offs between a and b permit greater variability in the inferred viscous Poisson ratio.

In summary, our results emphasize that the inferred rheological parameters (a, b, ν_v) should be interpreted as effective parameterizations of firn deformation within the present model framework. In particular, they capture the combined influence of processes such as grain rearrangement, grain-size-dependent creep, and evolving anisotropy, which are not explicitly represented. The inversion therefore diagnoses where the assumed rheology is incomplete, rather than directly recovering a unique, physically complete constitutive law. This perspective is consistent with classical phenomenological approaches to snow mechanics, in which the material is described in terms of effective viscous properties that depend on density and structure rather than a single fundamental mechanism (Salm, 1977).

https://doi.org/10.5194/egusphere-2026-3464
Preprint. Discussion started: 17 August 2026

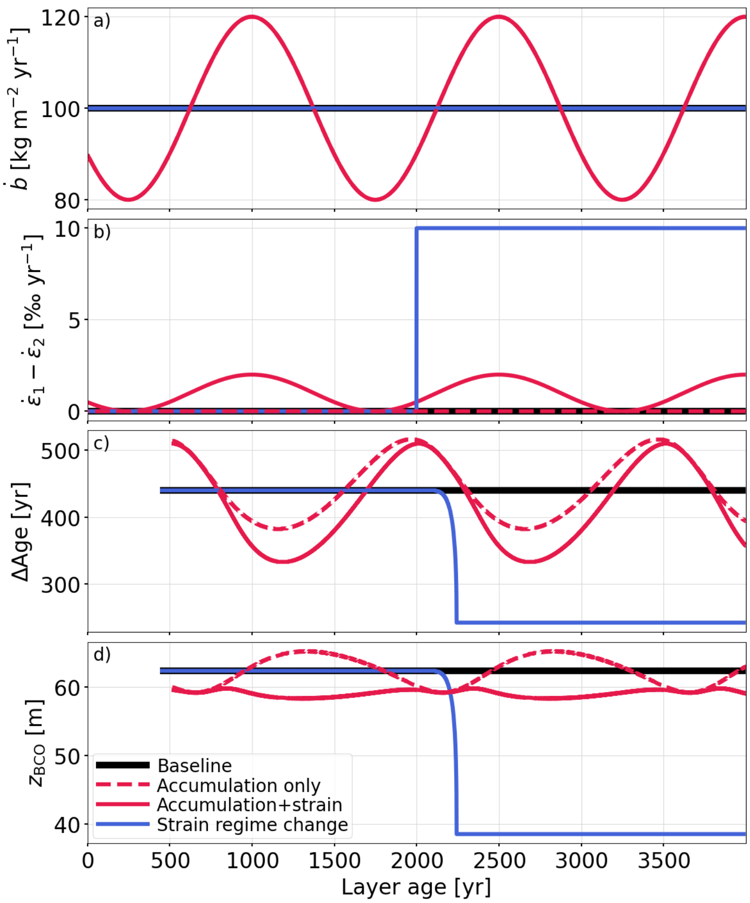

Figure 4. Effect of accumulation and horizontal strain variability on firn densification and gas-age proxies. (a) Accumulation rate, (b) shear strain, (c) Δage, and (d) bubble close-off (BCO) depth. Strain modifies both the mean state and variability of Δage, and regime changes produce shifts comparable in magnitude to climatic signals.

5.1 Impact of strain variability on firn proxies

To assess the implications of the inferred rheology for observable quantities, we consider a set of idealized experiments in which accumulation rate and horizontal strain are varied independently relative to a steady baseline case, while temperature and horizontal flow divergence are held constant (here fixed at $5 \times 10^{-4}\,\mathrm{yr}^{-1}$). The forcing varies on millennial timescales comparable to Dansgaard–Oeschger variability observed in ice-core records (Svensson et al., 2026) (Fig. 4). Bubble close-off (BCO) is defined here as the depth at which the firn density reaches $830\,\mathrm{kg\,m^{-3}}$, and Δage is calculated accordingly from the age difference between ice and air at this level.

The baseline case yields a steady-state close-off depth of approximately $62\,\mathrm{m}$ and a Δage of $440\,\mathrm{yr}$. When only accumulation is varied, the model shows strong sensitivity to burial rate, producing substantial variability in both z_{BCO} and Δage. Increased

https://doi.org/10.5194/egusphere-2026-3464
Preprint. Discussion started: 17 August 2026

burial reduces the time available for densification at shallow depths, shifting the balance between burial and compaction timescales and tending to push the close-off depth deeper. As a result, Δage varies between approximately 380 and $440\,\mathrm{yr}$. The response in Δage is also phase-shifted relative to the forcing, reflecting the fact that densification integrates the deformation history over time rather than responding instantaneously to surface conditions.

Including horizontal strain variability fundamentally changes the system response. Although the range in Δage remains large, variability in close-off depth is strongly reduced and the mean state shifts toward lower Δage. This reflects the distinct roles of the two forcings: accumulation alters the burial history, whereas strain directly modifies the densification rate through the full stress tensor. As a result, the response is governed not only by burial but also by deformation.

This effect is most clearly illustrated by an idealized regime-change experiment, in which the strain rate transitions from high to low shear while accumulation remains constant. The transition produces an increase in BCO depth of $\sim\ 24\,\mathrm{m}$ and a decrease in Δage of $\sim\ 200\,\mathrm{yr}$, reflecting the change in densification rates associated with the evolving stress regime. These changes are comparable in magnitude to those typically attributed to climatic forcing, despite the absence of any change in accumulation or temperature.

A useful perspective on the magnitude of this effect can be obtained from its impact on δ^{15}N through gravitational fractionation in the firn column (e.g. Schwander and Stauffer, 1984; Buizert et al., 2015). A shift in close-off depth of 20 m at $T \approx -31\,^{\circ}\mathrm{C}$ corresponds to a change in δ^{15}N of approximately $0.1\,‰$. Interpreted purely in terms of temperature, this would correspond to an apparent change of roughly 3–5 K, based on typical firn sensitivities of δ^{15}N to thermal fractionation of order 0.02–$0.03\,‰\,\mathrm{K}^{-1}$ (Grachev and Severinghaus, 2003).

Such behavior is consistent with evidence for past changes in ice dynamics. In northeast Greenland, Franke et al. (2022) identify a paleo–ice-stream system that has since been deactivated and replaced by a different drainage configuration, demonstrating that strain regimes can change substantially over time at fixed locations within an ice sheet. These results suggest that such transitions would leave a pronounced imprint on firn structure and gas-age proxies.

An intriguing implication is that firn-derived gas proxies may encode information about past deformation history. In regions affected by changes in ice-flow regime, measurements of δ^{15}N and related proxies could, in principle, be combined with independent accumulation constraints to infer aspects of past strain variability. Although inherently non-unique and model dependent, this highlights a pathway for using ice-core data to constrain both past climate and ice dynamics.

Because Δage and related gas-derived quantities are widely used to infer past surface conditions (Buizert et al., 2015; Buizert, 2021), this sensitivity has important implications for the interpretation of ice-core records. Our experiments show how changes in horizontal strain alone could produce shifts in Δage comparable to those associated with accumulation variability, implying that firn-derived proxies such as Δage and δ^{15}N may contain a dynamical component linked to ice-flow evolution.

Estimates of the interhemispheric phasing of Dansgaard–Oeschger cycles are larger when based on gas synchronization than when derived from volcanic matching (Svensson et al., 2026), with differences on the order of $\sim$150 yr. Because gas-based synchronization depends on Δage, it is sensitive to firn processes. The results presented here show that plausible changes in strain regime can produce variations in Δage of similar magnitude, potentially contributing to discrepancies in inferred

https://doi.org/10.5194/egusphere-2026-3464
Preprint. Discussion started: 17 August 2026

phasing. This highlights the potential for horizontal strain to influence gas-derived chronologies independently of atmospheric forcing and underscores the need to account for ice-dynamical effects when interpreting firn-derived climate proxies.

6 Conclusions

We develop a pseudo-steady-state firn column model and a Lagrangian flowline formulation to describe firn densification under horizontal strain. The steady-state model represents constant forcing, whereas the flowline model accounts for time-dependent accumulation and strain along particle trajectories, linking density profiles to deformation history within a one-dimensional framework. In this form, the rheology can be written in closed form and readily implemented in existing firn models (e.g. Stevens et al., 2020).

Combined with a spline-based inversion, this approach allows rheological parameters to be inferred as smooth, density-dependent functions without prescribed forms. The use of two sites with contrasting strain regimes but similar climatic forcing provides complementary constraints, reducing the degeneracy inherent to single-site inversions.

As a result, $r(\rho)$ is robustly constrained, whereas $a(\rho)$, $b(\rho)$, and $\nu_v(\rho)$ remain less well resolved. This reflects a fundamental limitation that firn-density profiles primarily constrain effective parameter combinations rather than their unique decomposition. The two inversion approaches agree in first-order behaviour but differ in detail due to these identifiability limits.

The inferred rheology departs from prior models (Gagliardini and Meyssonnier, 1997; Zwinger et al., 2007), indicating that firn deformation reflects multiple mechanisms rather than a single power-law description (e.g. Arnaud et al., 2000; Fourteau et al., 2024). Horizontal strain emerges as a first-order control on densification, implying that rheological parameters inferred from density profiles represent effective quantities.

The results further demonstrate that firn-density profiles cannot be interpreted independently of deformation history. Changes in strain regime alone can produce Δage variations comparable to climatic signals, suggesting that firn-derived proxies such as Δage and δ^{15}N may contain a dynamical component linked to ice-flow evolution.

These findings highlight the need to account for ice dynamics when interpreting firn structure and gas-age proxies.

Code and data availability. Code and data products generated for this study are available at: github.com/grinsted/grinsted_firn_model-publication-package. We intend to archive a final version of these materials upon manuscript acceptance. This study additionally relies on the following publicly available datasets: accumulation radar data from CReSIS (2014, files IRACC1B_20140515_02_099–107); EastGRIP density measurements from Rasmussen et al. (2023); the EastGRIP timescale from Sinnl et al. (2022); the ArcticDEM v3 elevation model (Porter et al., 2022); ice velocity products from TSX and DTU (Hvidberg et al., 2020; Andersen et al., 2020); and density profiles from Riverman et al. (2019).

https://doi.org/10.5194/egusphere-2026-3464
Preprint. Discussion started: 17 August 2026

Appendix A: Regional accumulation rates

A simple, externally constrained accumulation model is used to prescribe upstream variability. Spatial variability in accumulation upstream of EastGRIP is influenced by surface topography, with accumulation preferentially enhanced on windward slopes and reduced on leeward slopes. Vallelonga et al. (2014) showed that accumulation rates in the Northeast Greenland Ice Stream vary systematically with surface undulations at wavelengths of a few kilometers, consistent with wind-driven redistribution and preferential deposition (see also Dattler et al., 2019).

To quantify this variability along the upstream flowline, we trace a clear but shallow (∼15 m depth) radar isochrone in Operation IceBridge accumulation radar data acquired on 15 May 2014 (CReSIS, 2014). The shallow depth minimizes sensitivity to firn compaction uncertainties while preserving sufficient spatial coherence to resolve accumulation gradients.

We do not date the radar isochrone or apply a density correction correction to convert layer two way travel times to accumulation rates. Rather, the inferred accumulation history is scaled such that the mean accumulation rate over the past 1000 years along the profile matches an independent estimate derived from the EastGRIP ice core. This estimate is obtained by calculating the mass of each annual layer using the chronology of Sinnl et al. (2022) together with the density record of Rasmussen et al. (2023). Layer masses are converted to accumulation rates by accounting for the inferred layer-thinning from accumulated upstream flow divergence.

Spatial variability in accumulation is related to surface topography derived from ArcticDEM (Porter et al., 2022) using a linear regression model. Guided by earlier studies (Vallelonga et al., 2014), the predictors include surface slope, local elevation anomalies, and large-scale spatial gradients. The fitted model takes the form

$$\dot{b} = 108 + 1.4 \times 10^{-3}\,(S_s - S) \tag{A1}$$

$$\quad + 1.6 \times 10^{3}\,\nabla_x S_s + 7.5 \times 10^{2}\,\nabla_y S_s \tag{A2}$$

$$\quad + 1.0 \times 10^{-1}\,(x - x_0) - 5.9 \times 10^{-2}\,(y - y_0) \tag{A3}$$

where $\dot{b}$ is the accumulation rate, S is the surface elevation, and S_s is smoothed with a 2500 m Gaussian kernel. The terms $\nabla_x S_s$ and $\nabla_y S_s$ denote surface slopes in the x and y directions, and (x_0, y_0) is the location of EastGRIP. All quantities are expressed in units of kg, m, and yr.

Regression coefficients are estimated by minimizing the misfit between modeled and radar-derived accumulation rates along the IceBridge profile, after advecting observations 50 years upstream along back-trajectories. The resulting accumulation field (Fig. A1) captures the dominant variability associated with kilometer scale topographic steering of snowfall and wind driven redistribution, while remaining sufficiently simple for application along the reconstructed flowline. The model reproduces the radar-derived accumulation estimates with a root mean square misfit of 3.2 mm ice equivalent per year and explains a large fraction of the observed variance ($R^2 = 0.87$), indicating that the primary spatial patterns are well represented.

https://doi.org/10.5194/egusphere-2026-3464
Preprint. Discussion started: 17 August 2026

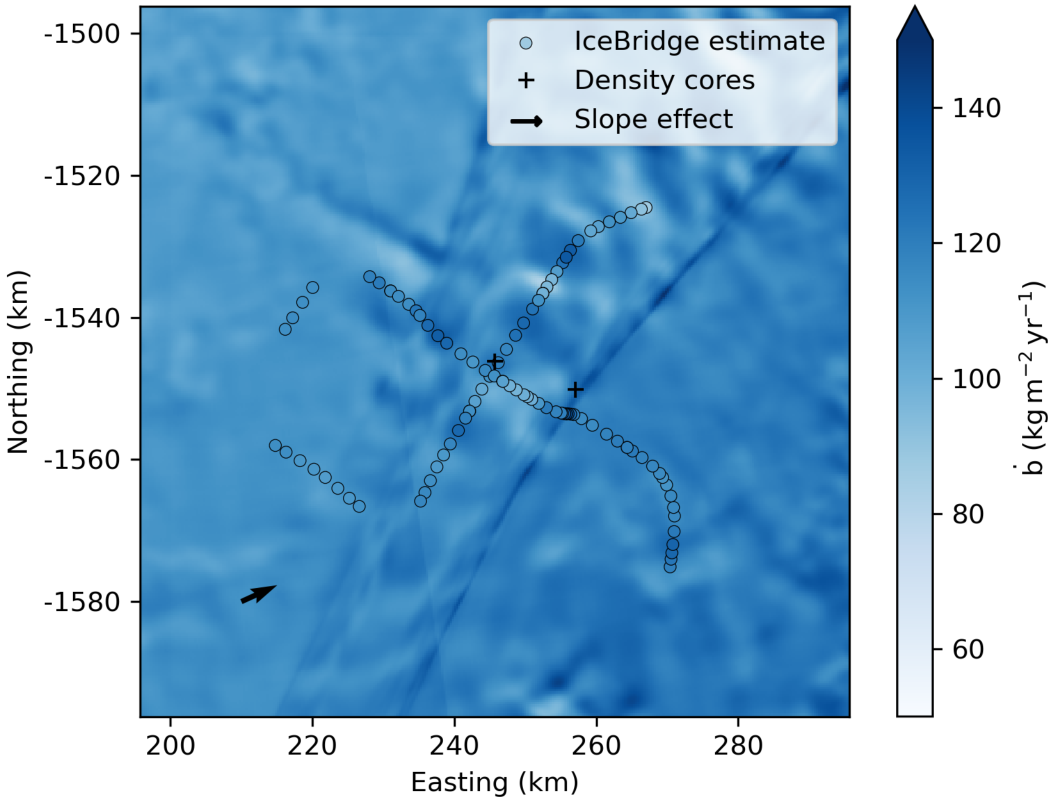

Figure A1. Regional accumulation rates obtained by regressing topographical features against local IceBridge-derived accumulation rates (circles). The direction of the surface slope regression coefficients is indicated by the arrow, and is consistent with the predominant wind direction.

Appendix B: Seasonal temperatures in a steady-state model

The implication of the non-linear rate factor is that compaction will be much faster during summer than during winter near the surface where temperatures at some sites can vary by more than 50 K over the year. As a consequence $A(\bar{T}) < \overline{A(T)}$ for temporally changing temperatures, where the overbar indicates the average over a year. Because of the nonlinear Arrhenius dependence, this approximation leads to a systematic underestimation of the effective rate factor in the presence of seasonal temperature variability. This is a concern for steady-state models, as most physically based firn densification models evaluate the rate factor at the mean annual temperature (e.g. Arthern et al., 2010; Goujon et al., 2003; Barnola et al., 1991), and might explain why Herron-Langway (Herron and Langway Jr, 1980) performs poorly when driven by temporally varying

https://doi.org/10.5194/egusphere-2026-3464
Preprint. Discussion started: 17 August 2026

temperatures (Arthern et al., 2010). We account for this effect in the steady-state model. We therefore first derive how the seasonal temperature amplitude decays with depth and use this to estimate $\overline{A(T)}$.

The implication of the non-linear rate factor is that compaction will be much faster during summer than during winter near the surface where temperatures at some sites can vary by more than 50 K over the year. As a consequence $A(\bar{T}) < \overline{A(T)}$ for temporally changing temperatures, where the overbar indicates the average over a year. This is a concern for steady-state models and might explain why Herron and Langway Jr (1980) performs poorly when driven by temporally varying temperatures (Arthern et al., 2010). We account for this effect in the steady-state model. We therefore first derive how the seasonal temperature amplitude decays with depth and use this to estimate $\overline{A(T)}$.

The advection-diffusion equation for temperature can be written as

$$\rho c \frac{DT}{Dt} = \frac{\partial}{\partial z} k \frac{\partial T}{\partial z} \tag{B1}$$

where c is the specific heat capacity, and the conductivity, k, is a function of ρ. Several parameterizations for $k(\rho)$ are available in the literature. Here, we adopt a standard formulation consistent with Arthern et al. (2010), noting that the precise choice has only a minor influence on the attenuation of seasonal temperature signals at depth. For the specific heat capacity we use (Fukusako, 1990) For 1D flow, this becomes

$$\rho c \frac{\partial T}{\partial t} = k \frac{\partial^2 T}{\partial z^2} - \left(\rho c w - \frac{\partial k}{\partial z} \right) \frac{\partial T}{\partial z} \,. \tag{B2}$$

For convenience, we define $\gamma \equiv \rho c w - \frac{\partial k}{\partial z}$.

We seek to describe how the amplitude of the seasonal temperature signal decays with depth. Rather than assuming a global solution to Eq. (B2), we adopt a *local approximation* in which material properties and vertical velocity vary slowly with depth. In this limit, the temperature field at a given depth can be expressed as a harmonic seasonal signal with a slowly varying amplitude,

$$T(t,z) = T_m + \Re\left\{ T_s(z)\, e^{i\omega t} \right\}, \tag{B3}$$

where $T_s(z)$ is a complex amplitude that varies with depth and encodes both attenuation and phase shift. We further assume that the complex amplitude varies locally as

$$T_s(z) \sim \exp(-e_z z + i k_z z)\,,$$

where e_z represents amplitude decay and k_z encodes the vertical phase shift.

To describe the attenuation of the seasonal signal, we introduce a local decay rate $e_z(z)$, defined through

$$\frac{\partial T_s}{\partial z} = -e_z(z)\, T_s(z). \tag{B4}$$

Substituting this form into Eq. (B2) and assuming that coefficients vary slowly with depth yields a local algebraic relation for the complex amplitude. Inserting Eq. B3 into Eq. B2 yields:

$$i \rho c \omega = (e_z + k_z i)(\gamma + e_z k + k k_z i)\,. \tag{B5}$$

https://doi.org/10.5194/egusphere-2026-3464
Preprint. Discussion started: 17 August 2026

Separating the real and imaginary parts, we get:

$$k_z^2 = e_z^2 + \frac{\gamma e_z}{k}$$

$$\rho c \omega = k_z(\gamma + 2 e_z k)$$

Isolating e_z from the second equation and substituting into the first yields a quadratic equation for k_z^2, which can be solved analytically to give

$$k_z^2 = \frac{-\gamma + \sqrt{\gamma^2 + 4(\rho c \omega)^2}}{4k} \,. \tag{B6}$$

The positive root is taken to ensure $k_z^2 > 0$ and physically meaningful attenuation of the temperature signal with depth. With k_z determined, the seasonal amplitude decay with depth becomes

$$e_z = \frac{\sqrt{4(k k_z)^2 + \gamma^2} - \gamma}{2k} \,. \tag{B7}$$

We can now calculate the decay of the seasonal amplitude with depth using equation B4.

The annual average value of A for a sinusoidal temperature is

$$\bar{A} = \frac{1}{\pi} \int_0^{\pi} A\left(T_m + T_s \cos(t)\right) dt \tag{B8}$$

We have not found an analytic expression for this integral. However, a good approximation can be found by making a third-order Taylor expansion of the Arrhenius exponent (Eq. 16) around $t = 0$. I.e. at the summer peak which dominates the annual average for large amplitudes. We write

$$\bar{A} \approx A(T_m + T_s)\, \frac{1}{\pi} \int_0^{\pi} \exp\left(-\frac{Q T_s t^2}{2R(T_m + T_s)^2}\right) dt \tag{B9}$$

$$= A(T_m + T_s)\, \frac{T_m + T_s}{\sqrt{2\pi Q R^{-1} T_s}}\, \mathrm{erf}\left(\frac{\pi\sqrt{Q R^{-1} T_s/2}}{T_m + T_s}\right) \tag{B10}$$

Often the form of $A(T)$ is chosen to be more complicated than a simple Arrhenius relationship, e.g. with an increased activation energy above $-10\,^\circ$C (Greve and Blatter, 2009). Such formulations are commonly used in modern firn and ice-flow models (e.g. Arthern et al., 2010; Ligtenberg et al., 2011). Eq. B10 is still a good approximation if we use an effective activation energy $Q' = \frac{d \log A}{dT} R T^2$. In practice, for an arbitrary rate factor function, we recommend calculating Q' using finite differences over the summer half of the seasonal cycle. Alternatively, $\bar{A}$ can be calculated by numerical integration.

Appendix C: Steady-state implementation

The steady-state firn-density profile can be calculated given the following material constants: $a(\rho)$, $b(\rho)$, $k(\rho)$, c, and $n = 3$, along with the site-specific parameters: $\dot{b}$, $\dot{\epsilon}_1$, $\dot{\epsilon}_2$, T_m, $T_s|_{z=0}$, and $\rho|_{z=0}$.

https://doi.org/10.5194/egusphere-2026-3464
Preprint. Discussion started: 17 August 2026

We obtain the steady-state density profile by integrating the governing equations downward from the surface using a finite-difference scheme with vertical step size Δz. At each depth level j, we track the evolution of density, overburden load, and seasonal temperature amplitude. The numerical procedure proceeds as follows:

1. Calculate the vertical stress σ_{zz} from the overburden load
2. Calculate the seasonal averaged $\bar{A}$ using Eq. B10
3. Calculate the vertical strain rate $\dot{\epsilon}_{zz}$ by solving Eq. 10
4. Calculate the vertical velocity w using Eq. 17.
5. Calculate the density gradient $\frac{\partial \rho}{\partial z}$ using Eq. 19
6. Calculate the thermal conductivity gradient using the chain rule, $\frac{\partial k}{\partial z} = \frac{\partial k}{\partial \rho}\frac{\partial \rho}{\partial z}$ (or estimate using upstream finite differences).
7. Calculate the seasonal temperature decay coefficient e_z using Eq. B7.
8. Update the state variables for the next layer ($j+1$):
   (a) Density: $\rho^{j+1} = \rho_{\text{ice}} - \exp\left[\log(\rho_{\text{ice}} - \rho^j) - \frac{\frac{\partial \rho}{\partial z}\Delta z}{\rho_{\text{ice}} - \rho^j}\right]$
   (b) Overburden load: $M^{j+1} = M^j + \frac{1}{2}(\rho^j + \rho^{j+1})\Delta z$
   (c) Temperature amplitude: $T_s^{j+1} = T_s^j e^{-e_z \Delta z}$

The density update rule (8a) ensures that ρ asymptotically approaches but never exceeds the ice density ρ_{ice}, regardless of the step size Δz. This is in contrast to a plain forward Euler scheme ($\rho^{j+1} = \rho^j + \frac{\partial \rho}{\partial z}\Delta z$), which can produce unphysical overshoots. The particular logarithmic transformation is motivated by empirical observations showing that the evolution of the density becomes approximately linear after a suitable nonlinear transformation (Herron and Langway Jr, 1980), improving both numerical stability and physical realism.

The explicit finite-difference scheme is stabilized by a natural negative feedback mechanism: if a density is overestimated at any depth, the resulting viscosity increase reduces the densification rate, naturally minimizing the impact of the error. Consequently, the numerical solution is relatively insensitive to the vertical step size Δz.

We note that the above scheme for computing steady-state profiles, accounting for both seasonal temperature variability and flow divergence, can be readily adapted to other densification models (such as Arthern et al., 2010) by modifying steps 3–5. Models formulated solely in terms of overburden stress can be further improved with the shear thinning correction of Oraschewski and Grinsted (2022) to better capture densification in high-shear environments, or by calculating the $\dot{\epsilon}_{zz}$-ratio with and without horizontal shear ($\dot{\epsilon}_1$ and $\dot{\epsilon}_2$) using Eq. 10.

https://doi.org/10.5194/egusphere-2026-3464
Preprint. Discussion started: 17 August 2026

Appendix D: Flowline model implementation

The flowline firn model extends the steady-state column formulation by solving the firn compaction equations in a time-dependent, Lagrangian framework. Firn layers are tracked as material volumes that evolve under time varying accumulation, overburden stress, and horizontal strain rates prescribed along a flowline.

Time is discretized at fixed intervals Δt, here chosen to be annual. At each time step a new surface layer is added representing one accumulation increment. Each layer i is characterized by the mass per unit horizontal area M_i, the density ρ_i, and its thickness $H_i = \frac{M_i}{\rho_i}$. Layer depths are diagnostic quantities computed from cumulative thickness. At each time step (t), we prescribe the accumulation rate ($\dot{b}(t)$), the surface density ($\rho_s(t)$), the horizontal principal strain rates ($\dot{\epsilon}_1(t)$, $\dot{\epsilon}_2(t)$). The temperature is kept constant.

At each time step, overburden stress (σ_{zz}) is computed from the cumulated overburden load. Given σ_{zz}, the prescribed horizontal strain rates, and the density-dependent rheological parameters (a and b), the vertical strain rate $\dot{\epsilon}_{zz}$ is obtained by solving the inverse Gagliardini flow law (Eq. 10).

Horizontal strain rates modify the mass per unit area of each layer through lateral convergence or divergence according to

$$\frac{DM}{Dt} = -M\left(\dot{\epsilon}_1 + \dot{\epsilon}_2\right) \, . \tag{D1}$$

This update is applied uniformly to all existing layers at each time step and represents the change in horizontal area of a material control volume. In practice, we use the following update rule: $M^{j+1} = M^j \exp\left(-(\dot{\epsilon}_1 + \dot{\epsilon}_2)\Delta t\right)$.

Density evolution follows the material form of mass conservation (see Eq. 8). Following the steady-state scheme (step 8a), density is updated using an implicit Herron–Langway–style transformation that ensures numerical stability and preserves the upper bound ρ_{ice}.

Appendix E: Inferred fabric from birefringence-induced loss

The first occurrence of a birefringence-induced loss, or beat, arises at the depth where the phase difference between the fast and slow waves reaches π. Young et al. (2021) provide a relation between phase difference and birefringence, here modified slightly to express it in terms of the eigenvalue difference $\Delta\lambda$ and adapted for firn conditions,

$$\phi \approx \frac{2\pi f_c}{c_0} \int\limits_0^{d(x)} \frac{\Delta\varepsilon' \, \Delta\lambda(x,z)}{\sqrt{\bar{\varepsilon}(x)}} \, dz \, , \tag{E1}$$

where c_0 is the speed of light in free space and $f_c = 750$ MHz (Rodriguez-Morales et al., 2014) is the radar center frequency. Here x denotes along-track distance and $d(x)$ the depth of the birefringence-induced loss. The quantity $\bar{\varepsilon}(x) = \frac{1}{d(x)} \int_0^{d(x)} \varepsilon(x,z) \, dz$ is the depth-averaged relative permittivity, and $\Delta\varepsilon' = 0.034$ (Matsuoka et al., 1997) is the birefringence of a single ice crystal.

https://doi.org/10.5194/egusphere-2026-3464
Preprint. Discussion started: 17 August 2026

In firn, the permittivity depends on density. We therefore estimate $\varepsilon(x,z)$ using density profiles derived from Riverman et al. (2019), combined with the DECOMP mixing model of Wilhelms (2005) to convert two-way travel time to depth and to compute $\bar{\varepsilon}(x)$.

Setting $\phi = \pi$ and assuming that $\bar{\varepsilon}(x)$ is approximately constant over the integration depth, Eq. E1 yields an estimate of the depth-averaged horizontal eigenvalue difference,

$$\pi = \frac{2\pi f_c}{c_0} \int_0^{d(x)} \frac{\Delta\varepsilon' \Delta\lambda(x,z)}{\sqrt{\bar{\varepsilon}(x)}} dz = \frac{2\pi d(x) f_c \Delta\varepsilon'}{c_0 \sqrt{\bar{\varepsilon}(x)}} \overline{\Delta\lambda}(x) \Rightarrow \overline{\Delta\lambda}(x) = \frac{c_0 \sqrt{\bar{\varepsilon}(x)}}{2d(x) f_c \Delta\varepsilon'}. \tag{E2}$$

The inferred birefringence signal and corresponding estimates of $\overline{\Delta\lambda}$ are shown in Fig. E1. Assuming a linear increase of $\Delta\lambda$ from an isotropic surface ($\Delta\lambda(0) = 0$), the observations imply values approaching $\Delta\lambda \approx 0.8$ at a two-way travel time of $0.26\,\mu$s ($\approx$ 24 m), indicating a strongly developed fabric at shallow depths.

Author contributions. AG conceived the study, developed the theory, developed the numerical implementation, and wrote the first draft of the manuscript. NMR derived the inverse rheology and assisted with interpreting the inferred coefficient functions. JF drilled and measured the shear margin core. NFN inferred fabric from radar observations. SOR assisted with the ice-core-derived accumulation rates. All authors contributed with discussions, and co-wrote the manuscript.

Competing interests. The authors declare no competing interests.

Acknowledgements. CH, AG, JLC, NMR received funding from the Novo Nordisk Foundation (NNF Challenge, PRECISE – Prediction of Ice Sheets on Earth, grant no. NNF23OC0081251). CH received funding from the European Union (Horizon Europe, ICELINK, grant no. 101184621). NFN received funding from the Novo Nordisk Foundation (ICE-SUSTAIN - Ice Cores for Sustainability, grant no. NNF24OC0088541). We would like to appreciate the work of icelab assistant Henning Ullrich and the drilling support by Daniela Jansen, Ole Zeising and Sepp Kipfstuhl.

EGRIP is directed and organized by the Centre for Ice and Climate at the Niels Bohr Institute, University of Copenhagen. It is supported by funding agencies and institutions in Denmark (A. P. Møller Foundation, University of Copenhagen), USA (US National Science Foundation, Office of Polar Programs), Germany (Alfred Wegener Institute, Helmholtz Centre for Polar and Marine Research), Japan (National Institute of Polar Research and Arctic Challenge for Sustainability), Norway (University of Bergen and Trond Mohn Foundation), Switzerland (Swiss National Science Foundation), France (French Polar Institute Paul-Emile Victor, Institute for Geosciences and Environmental research), Canada (University of Manitoba) and China (Chinese Academy of Sciences and Beijing Normal University).

AI-assisted tools was used to assist with language editing and improving clarity of the text.

https://doi.org/10.5194/egusphere-2026-3464
Preprint. Discussion started: 17 August 2026

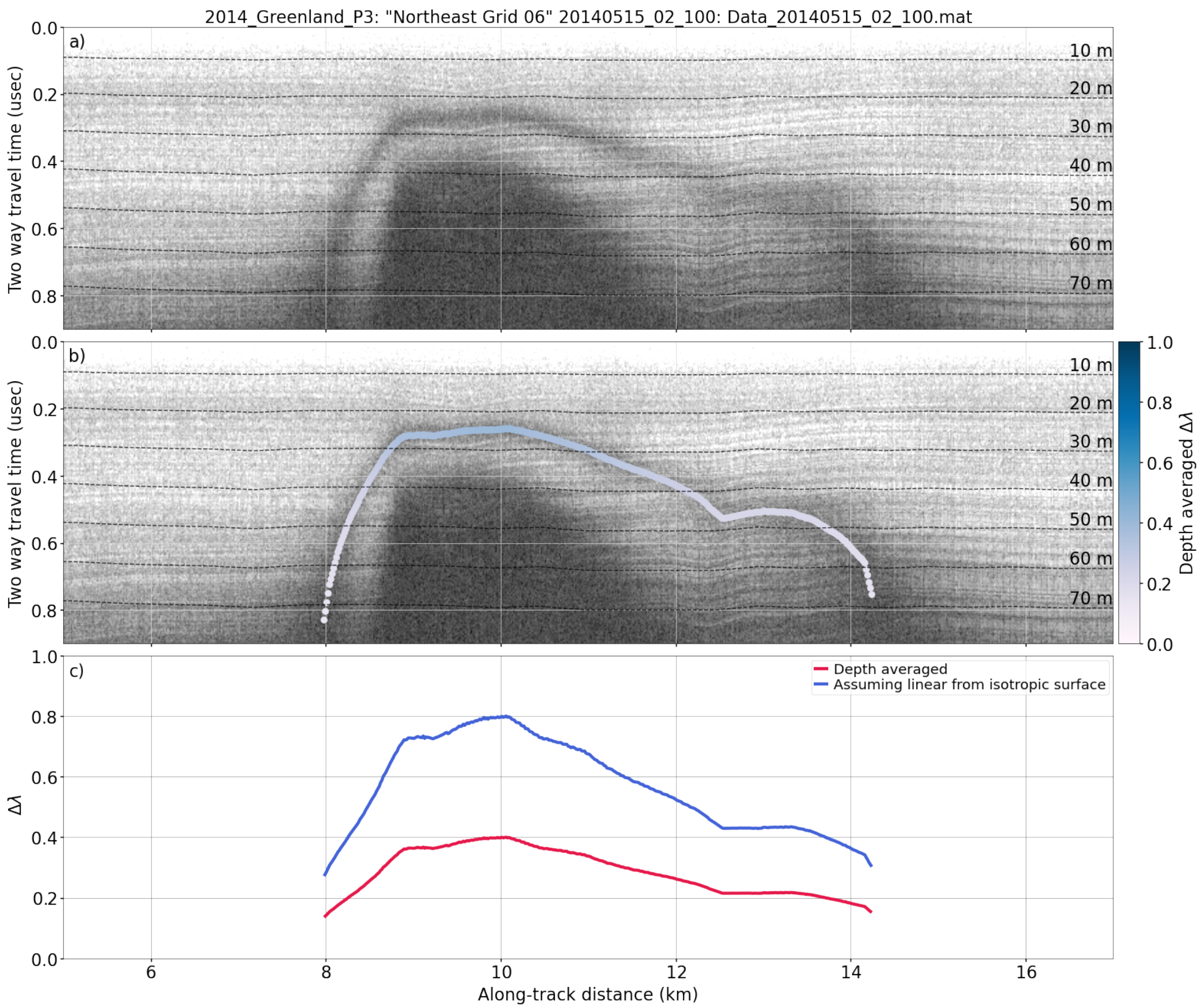

Figure E1. CReSIS accumulation radar data (CReSIS, 2014) and inferred fabric derived from birefringence-induced loss. (a) Radar data from the CReSIS accumulation radar (2014_Greenland_P3: "Northeast Grid 06", 20140515_02_100), showing clear evidence of fabric-induced birefringence loss. (b) Picked depths of birefringence loss, colored by the inferred depth-averaged horizontal eigenvalue difference. (c) Inferred depth-averaged eigenvalue difference (red), compared with the profile obtained assuming a linear increase of $\Delta\lambda(z)$ from an isotropic surface ($\Delta\lambda(0) = 0$).

References

Alley, R. B.: Firn Densification by Grain-Boundary Sliding: A First Model, Le Journal de Physique Colloques, 48, C1–256, https://doi.org/10.1051/jphyscol:1987135, 1987.

Andersen, J. K., Kusk, A., Boncori, J. P. M., Hvidberg, C. S., and Grinsted, A.: Improved Ice Velocity Measurements with Sentinel-1 TOPS Interferometry, Remote Sensing, 12, 2014, https://doi.org/10.3390/rs12122014, number: 12, 2020.

Arnaud, L., Barnola, J. M., and Duval, P.: Physical modeling of the densification of snow/firn and ice in the upper part of polar ice sheets, Physics of Ice Core Records, pp. 285–305, https://hdl.handle.net/2115/32472, 2000.

Arrizabalaga-Iriarte, J., Lejonagoitia-Garmendia, L., Hvidberg, C. S., Grinsted, A., and Rathmann, N. M.: Firn densification in two dimensions: modelling the collapse of snow caves and enhanced densification in ice-stream shear margins, Journal of Glaciology, pp. 1–48, https://doi.org/10.1017/jog.2025.6, 2025.

Arthern, R. J. and Wingham, D. J.: The Natural Fluctuations of Firn Densification and Their Effect on the Geodetic Determination of Ice Sheet Mass Balance, Climatic Change, 40, 605–624, https://doi.org/10.1023/A:1005320713306, 1998.

Arthern, R. J., Vaughan, D. G., Rankin, A. M., Mulvaney, R., and Thomas, E. R.: In situ measurements of Antarctic snow compaction compared with predictions of models, Journal of Geophysical Research: Earth Surface, 115, 2009JF001 306, https://doi.org/10.1029/2009JF001306, 2010.

Bader, H.: Theory of Densification of Dry Snow on High Polar Glaciers, II, U.S. Army Cold Regions Research and Engineering Laboratory, google-Books-ID: DHVdti2X_DUC, 1962.

Bagherzadeh, F., Freitag, J., Frese, U., and Wilhelms, F.: Resolution enhancement and segmentation of polar bubbly ice micro CT scans via 3D convolutional neural network, Applied Computing and Geosciences, 23, 100 193, https://doi.org/10.1016/j.acags.2024.100193, 2024.

Barnola, J. M., Pimienta, P., Raynaud, D., and Korotkevich, Y. S.: CO2-climate relationship as deduced from the Vostok ice core: a re-examination based on new measurements and on a re-evaluation of the air dating, Tellus B, 43, 83–90, https://doi.org/10.1034/j.1600-0889.1991.t01-1-00002.x, _eprint: https://onlinelibrary.wiley.com/doi/pdf/10.1034/j.1600-0889.1991.t01-1-00002.x, 1991.

Bartelt, P. and Lehning, M.: A physical SNOWPACK model for the Swiss avalanche warning: Part I: numerical model, Cold Regions Science and Technology, 35, 123–145, https://doi.org/10.1016/S0165-232X(02)00074-5, 2002.

Buizert, C.: The Ice Core Gas Age-Ice Age Difference as a Proxy for Surface Temperature, Geophysical Research Letters, 48, e2021GL094 241, https://doi.org/10.1029/2021GL094241, 2021.

Buizert, C., Cuffey, K. M., Severinghaus, J. P., Baggenstos, D., Fudge, T. J., Steig, E. J., Markle, B. R., Winstrup, M., Rhodes, R. H., Brook, E. J., Sowers, T. A., Clow, G. D., Cheng, H., Edwards, R. L., Sigl, M., McConnell, J. R., and Taylor, K. C.: The WAIS Divide deep ice core WD2014 chronology – Part 1: Methane synchronization (68–31 ka BP) and the gas age–ice age difference, Climate of the Past, 11, 153–173, https://doi.org/10.5194/cp-11-153-2015, 2015.

Chandel, C., Srivastava, P. K., and Upadhyay, A.: Estimation of Rheological Properties of Snow Subjected to Creep, Defence Science Journal, 57, 393–401, https://doi.org/10.14429/dsj.57.1786, 2007.

CReSIS: CReSIS Accumulation Radar data, Lawrence, Kansas, USA. Digital Media, http://data.cresis.ku.edu/, 2014.

Dattler, M. E., Lenaerts, J. T. M., and Medley, B.: Significant Spatial Variability in Radar-Derived West Antarctic Accumulation Linked to Surface Winds and Topography, Geophysical Research Letters, 46, 13 126–13 134, https://doi.org/10.1029/2019GL085363, _eprint: https://agupubs.onlinelibrary.wiley.com/doi/pdf/10.1029/2019GL085363, 2019.

Duva, J. and Crow, P.: Analysis of consolidation of reinforced materials by power-law creep, Mechanics of Materials, 17, 25–32, https://doi.org/10.1016/0167-6636(94)90011-6, 1994.

Fan, S., Wang, T., Prior, D., Breithaupt, T., Hager, T., and Wallis, D.: Flow laws for ice constrained by seventy years of laboratory experiments, https://doi.org/10.21203/rs.3.rs-4809184/v1, iSSN: 2693-5015, 2025.

https://doi.org/10.5194/egusphere-2026-3464
Preprint. Discussion started: 17 August 2026

Fausto, R. S., van As, D., Mankoff, K. D., Vandecrux, B., Citterio, M., Ahlstrøm, A. P., Andersen, S. B., Colgan, W., Karlsson, N. B., Kjeldsen, K. K., Korsgaard, N. J., Larsen, S. H., Nielsen, S., Pedersen, A. Ø., Shields, C. L., Solgaard, A. M., and Box, J. E.: Programme for Monitoring of the Greenland Ice Sheet (PROMICE) automatic weather station data, Earth System Science Data, 13, 3819–3845, https://doi.org/10.5194/essd-13-3819-2021, 2021.

Fourteau, K., Freitag, J., Malinen, M., and Löwe, H.: Microstructure-based simulations of the viscous densification of snow and firn, The Cryosphere, 18, 2831–2846, https://doi.org/10.5194/tc-18-2831-2024, 2024.

Franke, S., Bons, P. D., Westhoff, J., Weikusat, I., Binder, T., Streng, K., Steinhage, D., Helm, V., Eisen, O., Paden, J. D., Eagles, G., and Jansen, D.: Holocene ice-stream shutdown and drainage basin reconfiguration in northeast Greenland, Nature Geoscience, 15, 995–1001, https://doi.org/10.1038/s41561-022-01082-2, 2022.

Fukusako, S.: Thermophysical properties of ice, snow, and sea ice, International Journal of Thermophysics, 11, 353–372, https://doi.org/10.1007/BF01133567, 1990.

Gagliardini, O. and Meyssonnier, J.: Flow simulation of a firn-covered cold glacier, Annals of Glaciology, 24, 242–248, https://doi.org/10.3189/S0260305500012246, 1997.

Glen: The creep of polycrystalline ice, Proceedings of the Royal Society of London. Series A. Mathematical and Physical Sciences, 228, 519–538, https://doi.org/10.1098/rspa.1955.0066, 1955.

Goldsby, D. L.: Superplastic Flow of Ice Relevant to Glacier and Ice-Sheet Mechanics, in: Glacier Science and Environmental Change, pp. 308–314, John Wiley & Sons, Ltd, ISBN 978-0-470-75063-6, https://doi.org/10.1002/9780470750636.ch60, section: Sixty _eprint: https://onlinelibrary.wiley.com/doi/pdf/10.1002/9780470750636.ch60, 2006.

Goldsby, D. L. and Kohlstedt, D. L.: Superplastic deformation of ice: Experimental observations, Journal of Geophysical Research: Solid Earth, 106, 11 017–11 030, https://doi.org/10.1029/2000JB900336, _eprint: https://onlinelibrary.wiley.com/doi/pdf/10.1029/2000JB900336, 2001.

Goujon, C., Barnola, J.-M., and Ritz, C.: Modeling the densification of polar firn including heat diffusion: Application to close-off characteristics and gas isotopic fractionation for Antarctica and Greenland sites, Journal of Geophysical Research: Atmospheres, 108, https://doi.org/10.1029/2002JD003319, _eprint: https://agupubs.onlinelibrary.wiley.com/doi/pdf/10.1029/2002JD003319, 2003.

Grachev, A. M. and Severinghaus, J. P.: Laboratory determination of thermal diffusion constants for 29N2/28N2 in air at temperatures from -60 to 0°C for reconstruction of magnitudes of abrupt climate changes using the ice core fossil–air paleothermometer, Geochimica et Cosmochimica Acta, 67, 345–360, https://doi.org/10.1016/S0016-7037(02)01115-8, 2003.

Greve, R. and Blatter, H.: Dynamics of Ice Sheets and Glaciers, Advances in Geophysical and Environmental Mechanics and Mathematics, Springer Berlin Heidelberg, Berlin, Heidelberg, ISBN 978-3-642-03414-5 978-3-642-03415-2, https://doi.org/10.1007/978-3-642-03415-2, 2009.

Herron, M. M. and Langway Jr, C. C.: Firn Densification: An Empirical Model, Journal of Glaciology, 25, 373–385, https://doi.org/10.3189/S0022143000015239, 1980.

How, P., Lund, M., Ahlstrøm, A., Andersen, S., Box, J., Citterio, M., Colgan, W., Fausto, R., Karlsson, N., Jakobsen, J., Jakobsgaard, H., Larsen, S., Mankoff, K., Nielsen, R., Rutishauser, A., Shield, C., Solgaard, A., Stevens, I., van As, D., Vandecrux, B., Abermann, J., Bjørk, A., Langley, K., Lea, J., Messerli, A., and Prinz, R.: PROMICE and GC-Net automated weather station data in Greenland, https://doi.org/10.22008/FK2/IW73UU, 2022.

Hvidberg, C. S., Grinsted, A., Dahl-Jensen, D., Khan, S. A., Kusk, A., Andersen, J. K., Neckel, N., Solgaard, A., Karlsson, N. B., Kjær, H. A., and Vallelonga, P.: Surface velocity of the Northeast Greenland Ice Stream (NEGIS): assessment of interior velocities derived from satellite data by GPS, The Cryosphere, 14, 3487–3502, https://doi.org/10.5194/tc-14-3487-2020, 2020.

Joughin, I., Smith, B. E., and Howat, I. M.: A complete map of Greenland ice velocity derived from satellite data collected over 20 years, Journal of Glaciology, 64, 1–11, https://doi.org/10.1017/jog.2017.73, 2018.

Ligtenberg, S. R. M., Helsen, M. M., and van den Broeke, M. R.: An improved semi-empirical model for the densification of Antarctic firn, The Cryosphere, 5, 809–819, https://doi.org/10.5194/tc-5-809-2011, 2011.

Lundin, J. M. D., Stevens, C. M., Arthern, R., Buizert, C., Orsi, A., Ligtenberg, S. R. M., Simonsen, S. B., Cummings, E., Essery, R., Leahy, W., Harris, P., Helsen, M. M., and Waddington, E. D.: Firn Model Intercomparison Experiment (FirnMICE), Journal of Glaciology, 63, 401–422, https://doi.org/10.1017/jog.2016.114, 2017.

Matsuoka, T., Fujita, S., Morishima, S., and Mae, S.: Precise measurement of dielectric anisotropy in ice Ih at 39 GHz, Journal of Applied Physics, 81, 2344–2348, https://doi.org/10.1063/1.364238, 1997.

Mellor, M.: A Review of Basic Snow Mechanics, in: Proceedings of the Grindelwald Symposium, vol. 114, pp. 251 – 291, International Association of Hydrological Sciences, google-Books-ID: 4PtMQwAACAAJ, 1974.

Mellor, M. and Smith, J.: Creep of snow and ice, CRREL Res, Rep, 220, 13, 1966.

Oraschewski, F. M. and Grinsted, A.: Modeling enhanced firn densification due to strain softening, The Cryosphere, 16, 2683–2700, https://doi.org/10.5194/tc-16-2683-2022, 2022.

Porter, C., Morin, P., Howat, I., Noh, M.-J., Bates, B., Peterman, K., Keesey, S., Schlenk, M., Gardiner, J., Tomko, K., Willis, M., Kelleher, C., Cloutier, M., Husby, E., Foga, S., Nakamura, H., Platson, M., Wethington, M., Williamson, C., Bauer, G., Enos, J., Arnold, G., Kramer, W., Becker, P., Doshi, A., D'Souza, C., Cummens, P., Laurier, F., and Bojesen, M.: ArcticDEM, Version 3, https://doi.org/10.7910/DVN/OHHUKH, 2022.

Rasmussen, S. O., Vinther, B. M., Freitag, J., and Kipfstuhl, S.: EastGRIP snow-pack and ice-core densities (measured and modelled), https://doi.org/10.1594/PANGAEA.962754, 2023.

Riverman, K. L., Alley, R. B., Anandakrishnan, S., Christianson, K., Holschuh, N. D., Medley, B., Muto, A., and Peters, L. E.: Enhanced Firn Densification in High-Accumulation Shear Margins of the NE Greenland Ice Stream, Journal of Geophysical Research: Earth Surface, 124, 365–382, https://doi.org/10.1029/2017JF004604, 2019.

Rodriguez-Morales, F., Byers, K., Crowe, R., Player, K., Hale, R. D., Arnold, E. J., Smith, L., Gifford, C. M., Braaten, D., Panton, C., Gogineni, S., Leuschen, C. J., Paden, J. D., Li, J., Lewis, C. C., Panzer, B., Gomez-Garcia Alvestegui, D., and Patel, A.: Advanced Multifrequency Radar Instrumentation for Polar Research, IEEE Transactions on Geoscience and Remote Sensing, 52, 2824–2842, https://doi.org/10.1109/TGRS.2013.2266415, 2014.

Salamatin, A. N., Lipenkov, V. Y., Barnola, J. M., Hori, A., Duval, P., and Hondoh, T.: Snow/Firn Densification in Polar Ice Sheets, Low Temperature Science, 68, 195–222, https://hdl.handle.net/2115/45449, 2009.

Salm, B.: An Attempt to Clarify Triaxial Creep Mechanics of Snow, Physics of Snow and Ice : proceedings, 1, 857–874, https://eprints.lib.hokudai.ac.jp/dspace/handle/2115/20347, 1967.

Salm, B.: Snow Forces, Journal of Glaciology, 19, 67–100, https://doi.org/10.3189/S0022143000029221, 1977.

Schwander, J. and Stauffer, B.: Age difference between polar ice and the air trapped in its bubbles, Nature, 311, 45–47, https://doi.org/10.1038/311045a0, 1984.

https://doi.org/10.5194/egusphere-2026-3464
Preprint. Discussion started: 17 August 2026

Servén, D., Brummitt, C., Király, F., JodesL, Schmitz, D., Carmichael, Z., Ouslan, A., Miccoli, F., IlyesD, Taylor, J., Egan, J., Lapenta, L., Marín, L. S., Mo, S., Ranjan, S., Rose, S. A., Kraxner, T., Fasci, U., Szépe, V., Haddar, Y. E., hlink, Abedi, H., and nicoleta kyo: dswah/pyGAM: v0.12.0, https://doi.org/10.5281/zenodo.17981758, 2025.

Shinojima, K.: Study on the visco-elastic deformation of deposited snow, in: Physics of snow and ice, vol. 0, pp. 875–907, Institute of Low Temperature Science, Hokkaido University, http://hdl.handle.net/2115/20348, inst. Low. Temp. Sci, Hokkaido Univ., 1967.

Sinnl, G., Winstrup, M., Erhardt, T., Cook, E., Jensen, C. M., Svensson, A., Vinther, B. M., Muscheler, R., and Rasmussen, S. O.: A multi-ice-core, annual-layer-counted Greenland ice-core chronology for the last 3800 years: GICC21, Climate of the Past, 18, 1125–1150, https://doi.org/10.5194/cp-18-1125-2022, 2022.

Stevens, C. M., Verjans, V., Lundin, J. M. D., Kahle, E. C., Horlings, A. N., Horlings, B. I., and Waddington, E. D.: The Community Firn Model (CFM) v1.0, Geoscientific Model Development, 13, 4355–4377, https://doi.org/10.5194/gmd-13-4355-2020, 2020.

Svensson, A., Vettoretti, G., Lin, J.-m., Sinnl, G., Dahl-Jensen, D., Steffensen, J. P., Rasmussen, S. O., Vinther, B., Hvidberg, C., Kjær, H. A., Gkinis, V., Cook, E., Lohmann, J., Melcher, J. O., Halkjær, S., Kipfstuhl, S., Wilhelms, F., Adolphi, F., Fischer, H., Bigler, M., Sigl, M., Landais, A., Bouchet, M., Klüssendorf, A., Parrenin, F., Mulvaney, R., Wolff, E., Burke, A., Innes, H., Severi, M., Buizert, C., McConnell, J. R., Chellman, N., Wensman, S., Beer, J., Oyabu, I., and Muscheler, R.: Bipolar volcanic ice-core synchronization of the entire last glacial period, Quaternary Science Reviews, 375, 109 755, https://doi.org/10.1016/j.quascirev.2025.109755, 2026.

Vallelonga, P., Christianson, K., Alley, R. B., Anandakrishnan, S., Christian, J. E. M., Dahl-Jensen, D., Gkinis, V., Holme, C., Jacobel, R. W., Karlsson, N. B., Keisling, B. A., Kipfstuhl, S., Kjær, H. A., Kristensen, M. E. L., Muto, A., Peters, L. E., Popp, T., Riverman, K. L., Svensson, A. M., Tibuleac, C., Vinther, B. M., Weng, Y., and Winstrup, M.: Initial results from geophysical surveys and shallow coring of the Northeast Greenland Ice Stream (NEGIS), The Cryosphere, 8, 1275–1287, https://doi.org/10.5194/tc-8-1275-2014, 2014.

Vionnet, V., Brun, E., Morin, S., Boone, A., Faroux, S., Le Moigne, P., Martin, E., and Willemet, J.-M.: The detailed snowpack scheme Crocus and its implementation in SURFEX v7.2, Geoscientific Model Development, 5, 773–791, https://doi.org/10.5194/gmd-5-773-2012, 2012.

Wilhelms, F.: Explaining the dielectric properties of firn as a density-and-conductivity mixed permittivity (DECOMP), Geophysical Research Letters, 32, 2005GL022 808, https://doi.org/10.1029/2005GL022808, 2005.

Young, T. J., Schroeder, D. M., Jordan, T. M., Christoffersen, P., Tulaczyk, S. M., Culberg, R., and Bienert, N. L.: Inferring Ice Fabric From Birefringence Loss in Airborne Radargrams: Application to the Eastern Shear Margin of Thwaites Glacier, West Antarctica, Journal of Geophysical Research: Earth Surface, 126, https://doi.org/10.1029/2020jf006023, 2021.

Zwinger, T., Greve, R., Gagliardini, O., Shiraiwa, T., and Lyly, M.: A full Stokes-flow thermo-mechanical model for firn and ice applied to the Gorshkov crater glacier, Kamchatka, Annals of Glaciology, 45, 29–37, https://doi.org/10.3189/172756407782282543, 2007.